doi:10.26443/seismica.v5i1.1920

SEISMICA

Mapping the present-day 2-D crustal stress field and seismic moment release for the Greater Permian Basin of Texas as constrained by earthquake source mechanisms

Dino G.-C. Huang * [1], **Yangkang Chen** [1], **Alexandros Savvaidis** [1]

[1]Bureau of Economic Geology, The University of Texas at Austin, Austin, Texas, United States

Author contributions: *Conceptualization, Data Curation, Methodology, Investigation, and Writing (including the original draft, review, as well as editing)*: Dino Huang. *Data Curation*: Yangkang Chen. *Funding Acquisition*: Alexandros Savvaidis.

Abstract The greater Permian Basin is composed of three major subprovinces – the Delaware Basin, the Central Basin Platform, and the Midland Basin. Seismicity induced by fluid-injection in the basin has generated considerable seismic moment release. Notably seven M ≥ 5 earthquakes have been documented since 2017. To address the tectonic significance, in this study we collected previously published and newly determined focal mechanisms to invert for the regional stress model of the Permian Basin. We parameterized the model by 0.15° (longitude) x 0.1° (latitude) grid-spacing to group focal mechanisms for performing 2-D stress inversion, and used a trade-off curve to determine the optimal damper for regulating the model variation. We aimed to pursue a smooth gradient of the stress model and reveal the stress characteristics at the same time. Although the inversion results suggest that the Permian Basin contains an extensional stress field in general, the orientations of the principal stress axes are diverse within the basin. This heterogeneity further indicates that the two subprovinces of the Delaware and Midland Basins as well as the basement-rooted fault systems may not be subject to the same stress regime. We used seismic moment release as a proxy to evaluate the seismic deformation that resulted from induced seismicity. The fault systems located within the areas having higher seismic-moment release may have been previously stressed throughout an extended period of time, constituting a pre-existing elastic strain reservoir that accumulated considerable tectonic strains. Those strains are released by the present-day fault reactivation and induced seismicity.

Production Editor:
Andrea Llenos
Handling Editor:
Åke Fagereng
Copy & Layout Editor:
Miguel Neves

Signed reviewer(s):
Zoe Mildon

Received:
2025-08-07
Accepted:
2026-05-21
Published:
2026-06-29

1 Introduction

For decades, oil and gas activities of wastewater disposal (hereafter referred to as SWD) and hydrocarbon extraction (also known as hydraulic fracturing, hereafter referred to as HF-operation) have been very active in the Permian Basin of Texas. Both activities involve a considerable amount of pressurized fluid being injected into the underground sedimentary formations. During the HF-operation the fluid that is used to push out the oil and natural gas will flow back to the ground surface, whereas SWD simply injects the co-produced salt water into sedimentary formations. Changes in pore pressure through HF-operation and SWD have thus perturbed the local stress-state around pre-existing faults, triggering fault reactivation. Because of the on-going oil and gas activities, the fault reactivation has consequently resulted in very active induced seismicity. The focus of induced-seismicity studies for the Permian Basin has evolved over time. It began by reviewing the seismicity history and identifying/debating the nature of the seismicity – whether tectonic or induced (e.g., Frohlich et al., 2016), followed by a variety of topics: determination of the dominant causal factor – SWD or HF-operation (e.g., Grigoratos et al., 2022; Savvaidis et al., 2020), seismotectonics and mapping the seismogenic faults as deep basement-rooted and shallow strata-bounded (e.g., Horne et al., 2021, 2022, 2024; Huang et al., 2022, 2024; Huang and Savvaidis, 2024); pore-pressure management (e.g., Calle et al., 2024; Ge et al., 2024; Hennings et al., 2024), and hazard mitigation (e.g., Smye et al., 2024; Woo and Ellsworth, 2023).

Meanwhile, because of the increased seismicity, the Texas Seismological Network (TexNet) was established in 2017 to monitor earthquake activities in the State of Texas of the U.S., and provides earthquake catalogs to the public (Savvaidis et al., 2019). Prior to the establishment of TexNet, only several tens of M>3 earthquakes had been documented for the Permian Basin between 1931 and 2016 (The U.S. Geological Survey (USGS), 2025). Among them, only three earthquakes were having magnitudes ≥ 5.

The induced seismicity in the Permian Basin has been active in three broad regions: the Delaware Basin, the Midland Basin, and the Snyder area (Figure 1). The depth range of the induced seismicity is 0-15 km below mean sea level. Taking the relative depth to the basin-basement interface into account, a vast majority of the induced seismicity are located below the basin-

*Corresponding author: dino.huang@beg.utexas.edu

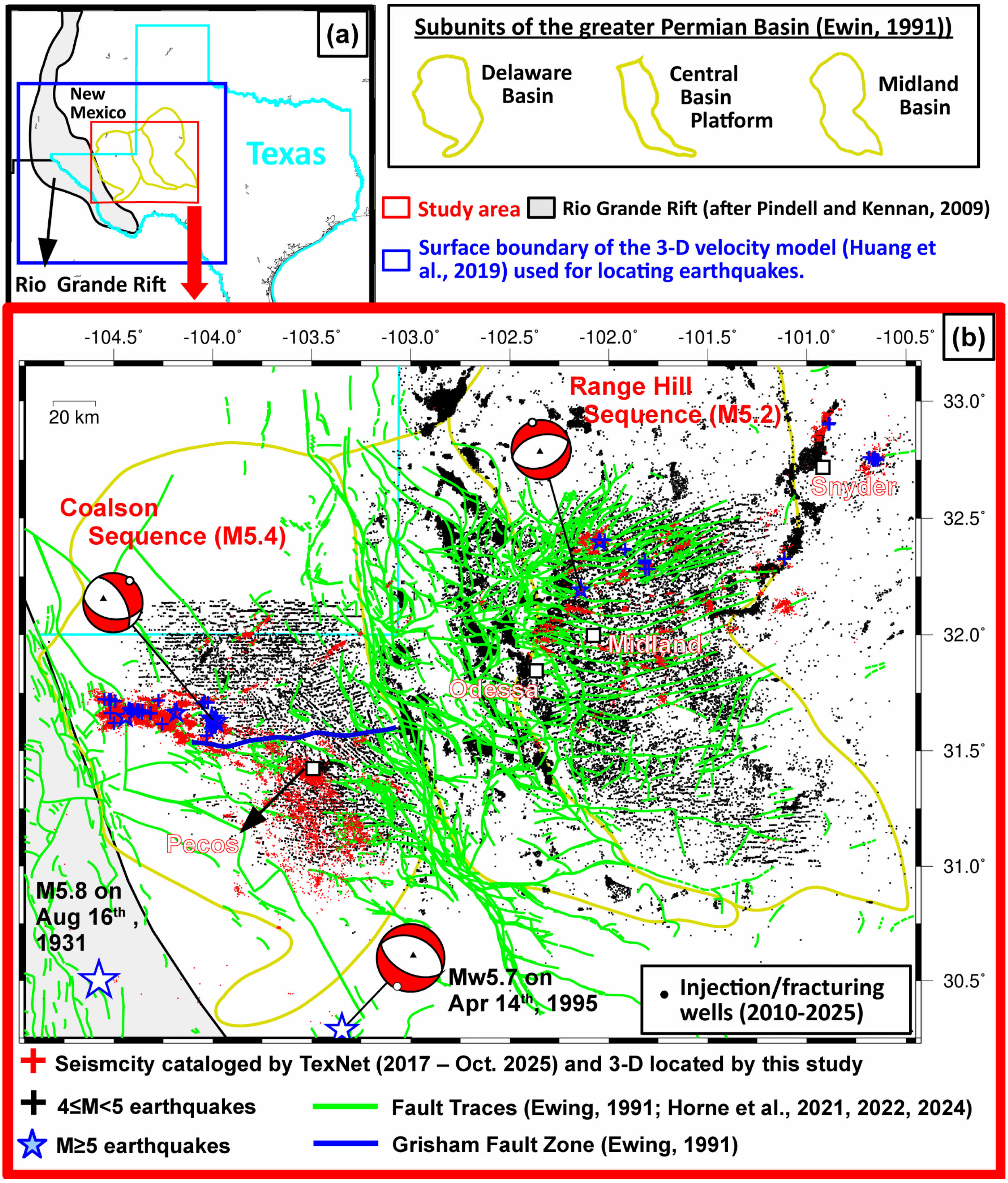

Figure 1 A composite figure shows the study area, seismicity distribution, and the tectonic map of the greater Permian Basin. Panel (a): The study area (bound by red line) and surface extent of a 3-D velocity model (Huang et al., 2019) that was used to refine earthquake hypocentral locations. Panel (b): A zoom-in figure of the study area and induced seismicity. The TexNet has documented over 34,274 M ≥ 1.0 events for our study area from 2017 to October 2025, including seven M ≥ 5 earthquakes (denoted by blue stars). Two focal mechanisms of M ≥ 5 earthquakes are of the normal faulting type (Huang et al., 2022, 2024). Two historical M5+ earthquakes occurred in adjacent to the Permian Basin (U.S. Geological Survey (USGS), 2025). One of them (M5.8) was within the Rio Grande Rift. The other (Mw5.7) was at the southern tip of the Delaware Basin. It is also of the normal faulting type.

basement interface (Huang et al., 2022, 2024; Huang and Savvaidis, 2024). Considering that the seismicity distribution is a proxy of seismogenic faults, the extent of induced seismicity thus suggests that these pre-existing seismogenic faults are rooted in the top portion of the crystalline Pre-Cambrian basement; most of which are previously unknown. In addition to 3-D seismic and geologic observations, the induced seismicity has thus provided seismologic constraints to enhance the effort on fault mapping (Horne et al., 2021, 2022, 2024). As a result, a large number of segmented faults have been discovered across the Permian Basin (Figure 1). In light of pressurized fluid-injection, the knowledge of the present-day crustal stress state and fault architectures is useful to forecast the faulting threshold and faulting type of future induced earthquakes. Efforts have been made to improve the knowledge of the stress state of the Permian Basin (e.g., Lund Snee, 2024). These efforts commonly used data of borehole breakouts to constrain the stress state. As a result, a compiled stress map (Lund Snee, 2024; Snee and Zoback, 2022) has suggested that the Permian Basin contains an extensional stress field. It also demonstrates a seemingly gradual-and-smooth transition of faulting types.

Despite a broadly homogeneous extensional stress field, the focal mechanisms and the spatial distribution of induced seismicity have shown a complex fault architecture across the Permian Basin: a very distinctive variation of seismogenic patterns. In the Delaware Basin, there is an observable change in the seismicity trend on either side of the basin-bisecting Grisham fault zone (GFZ). The extent of hypocentral depths vary drastically across the fault zone: while the focal mechanisms present predominantly normal faulting, there is a noticeable variation in hypocentral depths. To the north of the GFZ, earthquakes are deeper and commonly located below the basin-basement interface; meanwhile, the nodal planes of the focal mechanisms are collectively striking in an east-west direction. To the south of the GFZ, the earthquakes are located at a depth shallower than 7 km (Figure 2) and across the basin-basement interface, the collective strike of focal-mechanism nodal planes becomes NW-SE. In contrast, there is a very different seismotectonic pattern in the Midland Basin: a mix of strike-slip and normal faulting. Notably, a NE-SW stretching normal-faulting zone bisects the Midland Basin. Still, a vast majority of seismicity within the Midland Basin and the Snyder seismic zone are located in the crystalline basement.

Alternatively, for assessing the crustal stress state one can use earthquake focal mechanisms to infer the stress field because focal mechanisms are directly related to the stress that causes the earthquakes. For a seismically quiescent region with few naturally occurring tectonic earthquakes (e.g., the Permian Basin), the sheer number of induced earthquakes and their focal mechanisms have allowed us to map a detailed regional stress field with a better spatial resolution. To serve this purpose, in this study we collected the previously published focal mechanisms and added new focal mechanisms determined by this study to invert for a present-day regional stress model. In addition to assessing the stress state, the recently observed subsidence of the ground surface in parts of the Delaware Basin and a handful M ≥ 5 earthquakes across the Permian Basin have prompted a need to assess a long-term seismic deformation resulted from the induced seismicity. Particularly, it is worth noting that the accumulative vertical deformation has reached as much as nearly 13 cm of subsidence near the city of Pecos, Texas (from Nov 2014 through Jan 2019 Staniewicz et al., 2020).

Together, the obtained regional stress model and the density map of seismic moment-release allow for future assessment and mitigation of potential seismic hazards from the induced seismicity and the seismogenic structures.

2 Data analysis techniques

2.1 Refine earthquake hypocentral locations and group earthquake focal mechanisms

The TexNet started to monitor seismicity for the Permian Basin in 2017. For this study, we have selected 34,274 M ≥ 1.0 earthquakes (from 2017–Oct 2025 Bureau of Economic Geology, 2025) to refine their hypocentral locations by using a 3-D velocity model (referred to as PB3D; Huang et al., 2019). This PB3D model was developed by tomographic inversion, covering the greater Permian Basin and allowing for better constraints on hypocentral locations (referred to as "3-D located"). Subsequently we used the 3-D located hypocenters to group earthquakes that have focal mechanisms for stress inversion. For these earthquakes, we first collected published focal mechanisms from Huang et al. (2022, 2024) and Huang and Savvaidis (2024).

On top of the published focal mechanisms, we also determined new focal mechanisms for a better spatial coverage across our study area; and we followed the same approach of full-waveform moment tensor inversion (referred to as rCMT; Huang et al., 2024; Huang and Savvaidis, 2024) to determine new focal mechanisms. To select quality rCMT-based focal mechanisms for stress inversion, we set two criteria of the waveform misfit and the percentage of the double-couble component (DC) out of a full-moment tensor; where the minimum threshold of DC is 70% and threshold of waveform misfit is 0.8 (a minimum misfit = 0 represents the full waveform match between synthetic and observed data, and a maximum misfit = 2 indicates a total misfit between the two). To expand the database of focal mechanisms as much as possible, in addition to using waveform moment tensor inversion, we used HASH (a first-motion-polarity based approach; Hardebeck and Shearer, 2002, 2003) to determine focal mechanisms for earthquakes that have insufficient waveform quality for full waveform inversion but the data quality is sufficient to identify the first-motion polarities. For this purpose, we first used a machine-learning based algorithm (Chen et al., 2024) to identify the first-motion polarities and their amplitudes. The determination of focal mechanisms was thus constrained by the P-wave first-motion polarities and S/P wave-amplitude ratios. Afterwards, those HASH-determined focal mechanisms were manually reviewed to remove outliers. As the HASH provides quality assessment of focal mechanisms, we selected focal mechanisms of qualities A and B.

Staniewicz et al. (2020) and Hennings et al. (2023) attributed the ground subsidence to mainly the reduction of hydrocarbon content. Lee et al. (2023) further demonstrated that both reservoir compaction (due to the reduction of hydrocarbon content) and fault reactivation near the hydrocarbon reservoir have jointly contributed to the geodetically observed ground deformation. Specifically, the fault-slip has a more dominant effect than the compaction does.

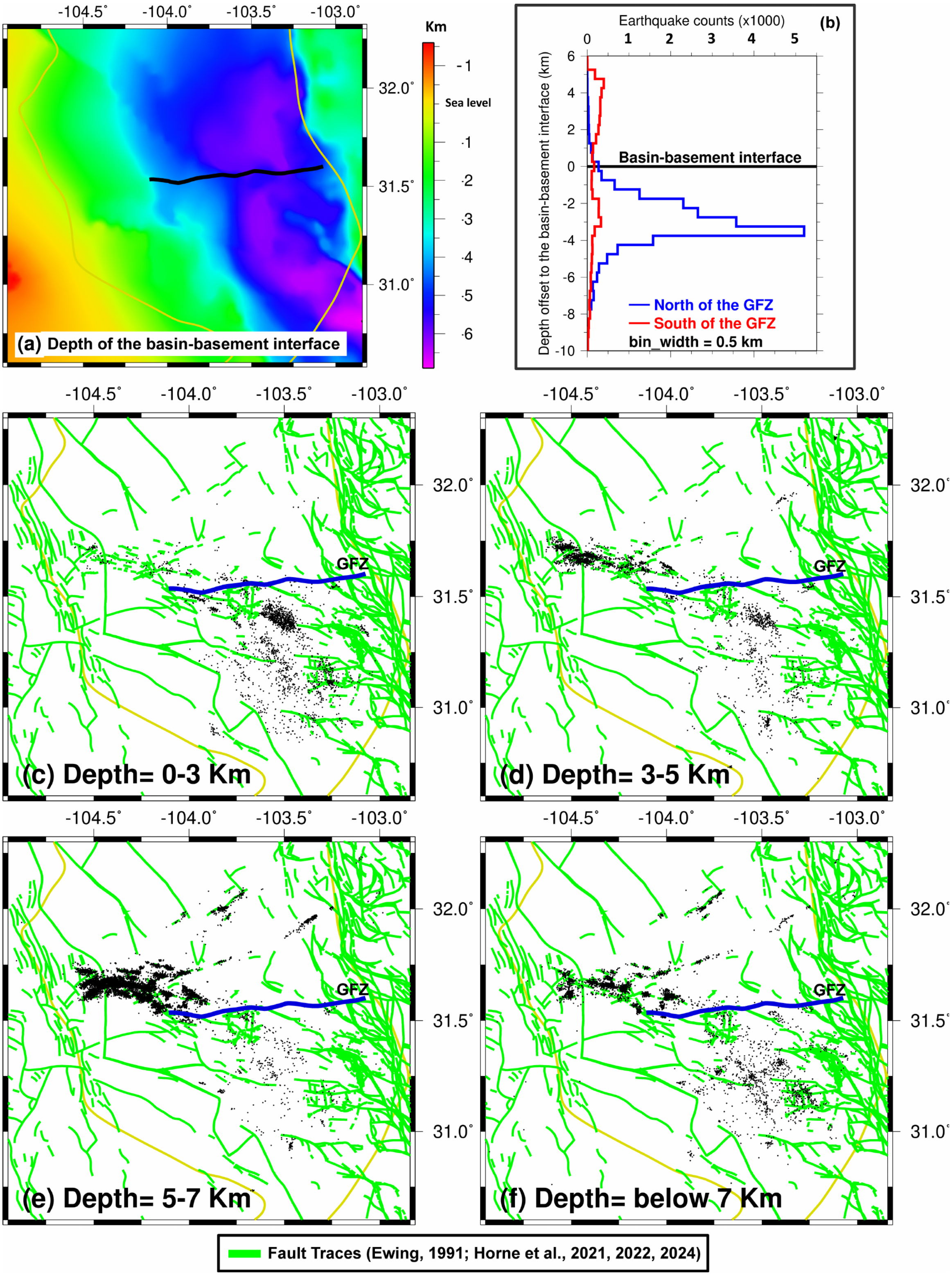

Figure 2 Panel (a) shows the topography of the basin-basement interface. Panel (b) shows the statistics of focal depth offset with respect to the basin-basement interface for earthquakes located north or south of the GFZ, respectively. Panels (c)-(f) show seismicity distribution within different depth layers. Across the Grisham Fault Zone (GFZ), the seismicity is present in different depth ranges. To the south of the GFZ, the earthquakes are located at a depth shallower than 7 km and across the basin-basement interface. North of the GFZ, earthquakes are deeper and commonly located below the basin-basement interface.

2.2 Stress Inversion

We parameterized a 2-D stress model by creating a set of grid-points with a spacing of 0.1° in latitude and 0.15° in longitude across the Permian Basin (Figure 2a). As we intended to pursue a smooth gradient of model parameters, we grouped available focal mechanisms that were located within a range of ±0.1° in latitude and ±0.15° in longitude for every grid-point. We used the Spatial and Temporal Stress Inversion algorithm (Hardebeck and Michael, 2006), which is based on a damped least-square inversion approach. It searches for a stress tensor for each grid-point, aiming to minimize the difference between the observed slip vectors from the focal mechanisms and the predicted shear stress orientations along the fault planes. It also tries to minimize the differences of the stress tensors between neighboring grid-points. Our inversion approach also bears two assumptions from the data set: (1) slip in earthquakes is parallel to the greatest resolved shear stress on the fault plane, and (2) stress is constant in space and time within each defined group of focal mechanisms. As in other geophysical inversion practices, cautions need to be taken to reduce artifacts introduced by insufficient data or noise existing within the data. Here we took two essential approaches at the same time to ensure the inversion stability: (1) Following the recommendation of Barth et al. (2008) and Yang and Hauksson (2013), we included more than 15 well-constrained focal mechanisms for the earthquake group at each grid-point. We excluded grid-points without enough focal mechanisms from inversion (Figure 2a); (2) Adopted a proper damper to regulate the model variation for achieving a smoother stress gradient across the region. This damping parameter can be determined from a trade-off curve between data misfit and model variation. Thus, we tested on a series of damping factors ranging from 0 to 20 at an increment of 0.02 to form the trade-off curve (Figure 2b).

After the stress inversion, we bootstrapped the model parameters to assess the robustness of inversion results. Assuming the 50% chance for fault planes being correctly picked, we set a 95% confidence level from 1000 bootstraps for each best-fitting parameter to evaluate the uncertainty of the inverted principal stress axes for the stress tensor of each grid point: (1) the maximum stress axis, S1 (i.e., the most compressional, approximately equivalent of P-axes from focal mechanisms), (2) the intermediate stress axis, S2 (i.e., intermediate compressional, approximately equivalent of B-axes from focal mechanisms), and (3) the minimum stress axis, S3 (i.e., the least compressional, approximately equivalent of T-axes from focal mechanisms). Lastly, we determined the stress ratio R (Angelier, 1979; Gephart and Forsyth, 1984) for each grid-point by using the equation of $R = (\sigma 1 - \sigma 2)/(\sigma 1 - \sigma 3)$, where $\sigma 1$, $\sigma 2$, and $\sigma 3$ are the eigen values of S1, S2 and S3, respectively. The maximum R is 1 and the minimum R is 0. Lastly, we followed the methods developed by Lund and Townend (2007) to estimate maximum horizontal shear-stress (SHmax) from the inverted stress tensors.

2.3 Converting earthquake local magnitude (ML) to seismic moment release

While seismicity can release seismic moment, the resulting seismic moment rate can also be considered as a proxy to evaluate the crustal deformation associated with the seismicity. To better characterize the released seismic moment from tens of thousands earthquakes that occurred in the last 9 years (2017-2025), we first translated the local magnitude (referred to as ML(TexNet); Kavoura et al., 2020) to moment magnitude (referred to as rCMT-Mw) using three different scaling equations (Huang et al., 2022, 2024; Huang and Savvaidis, 2024), depending on where each individual earthquake is located. The three equations are:

1. Delaware Basin (for earthquakes located west of -103° Longitude):

$$\mathrm{rCMT} - \mathrm{Mw} = 0.98 \times \mathrm{ML}(\mathrm{TexNet}) - 0.35 \quad (1)$$

2. Midland Basin (for earthquakes located between -103° and -101° Longitudes):

$$\mathrm{rCMT} - \mathrm{Mw} = 0.75 \times \mathrm{ML}(\mathrm{TexNet}) + 0.61 \quad (2)$$

3. Snyder area (for earthquakes located east of -101° Longitude):

$$\mathrm{rCMT} - \mathrm{Mw} = 0.73 \times \mathrm{ML}(\mathrm{TexNet}) + 0.58 \quad (3)$$

Next we converted these translated Mw to seismic moment (M0) by using: $\mathrm{Mw} = (2/3) \times log(\mathrm{M0}) - 10.73$ (Hanks and Kanamori, 1979), where M0 is in dyne-cm and we eventually converted the unit to N-m. Lastly, we used the same way of grouping the earthquake source mechanisms to group the seismicity. We aimed for calculating their total seismic-moment release (N-m), the seismic-moment rate (N-m/year), and the magnitude-frequency distribution (i.e., *b*-value) as a proxy to assess the state of seismicity. For determining the seismic moment rate at each earthquake group, we considered the time duration of seismicity (starting from the time when the first event was documented for the respective group) to be longer than 180 days for a meaningful temporal resolution. At the same time, for better statistic constraints, we set a threshold of minimum 100 earthquakes to determine the *b*-value of each earthquake group.

3 Results - the inverted 2-D stress model

We have compiled a database of 1591 focal mechanisms (a combination of both 836 rCMT- and 755 HASH-determined focal mechanisms), and effectively inverted for a 2-D regional stress model for areas across the Permian Basin of Texas. Consequently, the average uncertainty of trend is 15.7° for S1, 7.2° for S2, and 4.4° for S3 (Figure 2c). Meanwhile, the average uncertainty of plunge is 2.3° for S1, 2.6° for S2, and 2.4° for S3 (Figure 3c). Figure 4 illustrates examples of the stress inversion results for two grid-points that contain the M5.4 Coalson sequence and the M5.2 Range Hill sequence, respectively. The axial orientations of P- and T-axes from the focal mechanisms and the inverted stress axes (S1 and S3) are quite consistent for the respective grid-points. The obtained principal stress axes are listed in Table S1. In this section, we will characterize the stress model by the spatial distribution of the principal stress axes (S1 and S3), the stress ratio, SHmax , and the faulting types (Figures 5 and 6).

Figure 5 presents the spatial characteristics of S1 and S3 axes (trend and plunge) as well as the stress ratios from the inverted 2-D stress model. At a glance, S1 axes present a seemingly strong heterogeneity: the plunges vary from near vertical to low angles. And yet, the

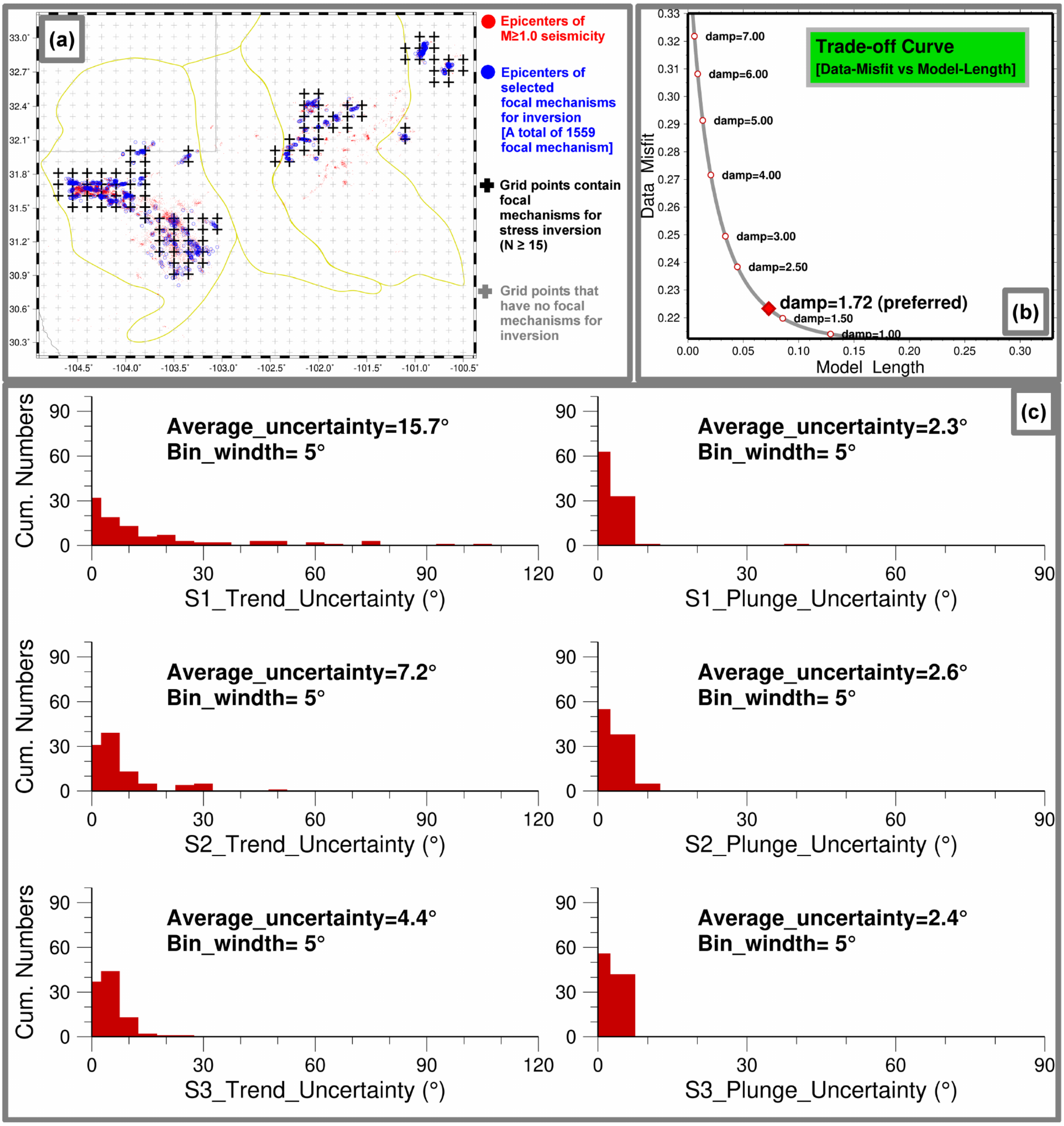

Figure 3 Composite figures show model parameterization for stress inversion and assessment of the inversion results: (a) Grid settings and the distribution of selected focal mechanisms; (b) Trade-off curve of the damper test for stress inversion. We used this curve to determine the optimal damper that can best balance the model length and data misfit; and (c) Histograms of uncertainty (orientation and plunge) for S1, S2, and S3.

S1 axes appear to be randomly oriented in various directions across our study area. However, when S1 is mostly near vertical (plunge > 70 °), its azimuth is less well defined. Therefore any small change of 3-D orientation from a near-vertical S1 will present a seemingly large change in the projected azimuth on the focal sphere. Thus, we expect seemingly large scattering of S1 azimuths existing in areas with a mix of normal and oblique-normal faulting. Caution needs to be taken when interpreting these variations.

The S3 axes are commonly horizontal across the Permian Basin, where the trend of S3 is gradually rotating from near N-S direction (in the area close to the border of New Mexico and Texas) to NE-SW direction (in the southern Delaware Basin). We have noticed that the GFZ, the most prominent tectonic feature in the Delaware Basin, appears to have no influence on the stress field. There is no noticeable discontinuity of stress orientation present in the stress field of the Delaware Basin. East of the Central Basin Platform, S3

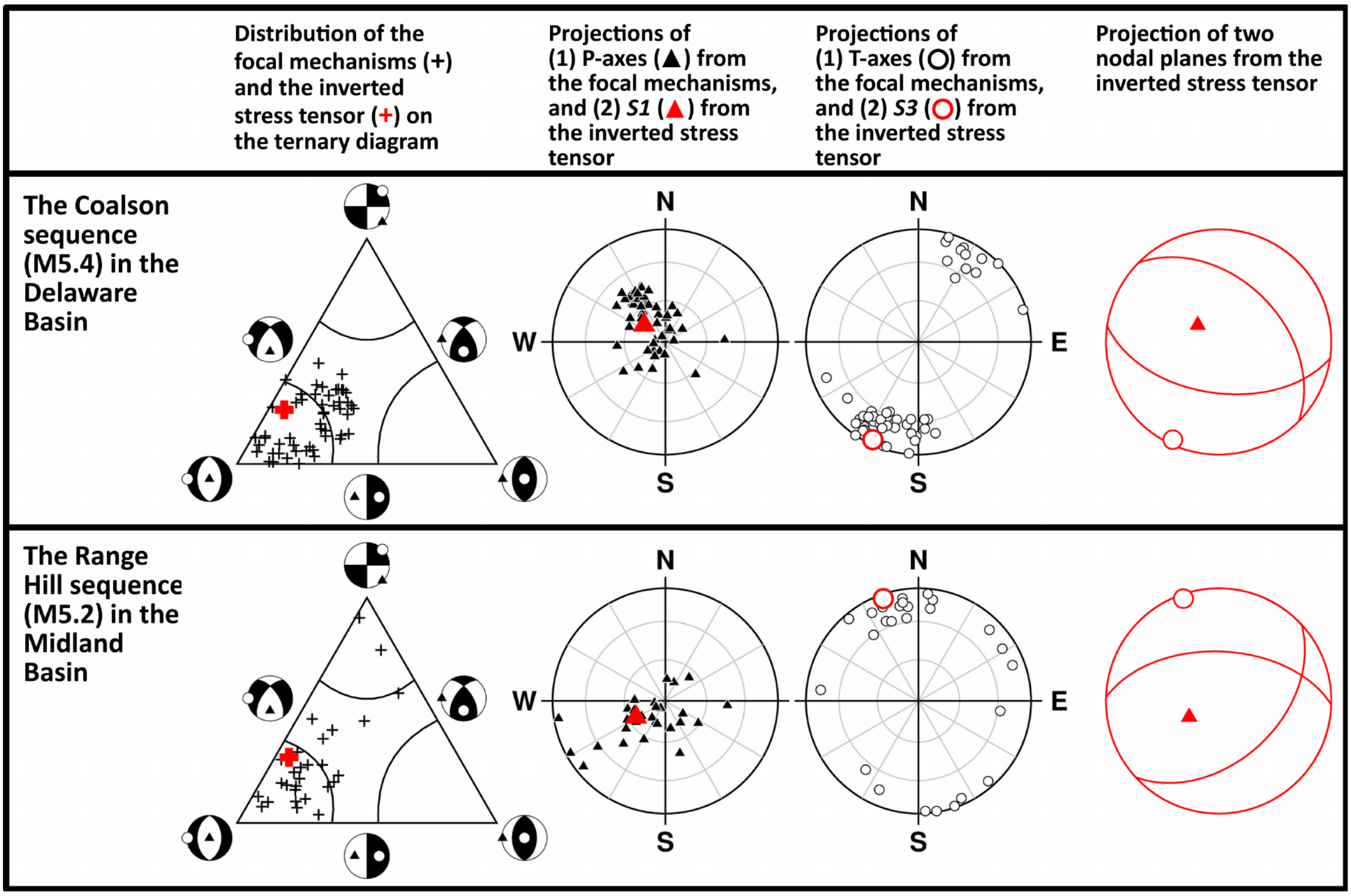

Figure 4 Examples show the stress inversion results for two grid-points that contain the Coalson (M5.4) and Ranch Hill (M5.2) sequences, respectively.

axes are consistently oriented in a northwest-southeast direction (around 330° azimuth) in the Midland Basin and the Snyder seismic zone. In addition, much of the stress ratios from our study area are around the peak level of R = 0.4–0.6. They however show a spatial pattern: generally higher (R = 0.4–0.8) in the Delaware Basin and generally lower (R = 0.1–0.5) in the Midland Basin. Specifically, we have observed a small area having much higher stress ratios (R = 0.6–0.8), located in the southeastern Delaware Basin. Nonetheless, the notion of an extensional stress field existing in the Permian Basin is consistent with the inference from the previous seismotectonic studies. From which, normal and strike-slip faulting together are accommodating the crustal extension.

Figure 6 uses the color-coded ternary diagram (modified from Frohlich and Apperson, 1992) to demonstrate the prospective faulting type of each respective stress tensor. As opposed to the conventional Anderson's faulting parameter – AΦ (Anderson, 1905; Simpson, 1997) for defining the faulting type that only allows one dimensional transformation from normal to thrust faulting (or vice versa), this approach takes the plunges of three principal stress axes into account and allows for a two-dimensional transformation of faulting types on the diagram. For example, the faulting type can be transformed from normal to thrust faulting via vertical dip-slip faulting, without necessarily going through the strike-slip faulting required by using AΦ. It is worth noting that the distribution of prospective faulting types corroborates the observations of focal mechanisms. Still, the Delaware and Midland Basins have very different faulting behaviors: the faulting in the Delaware Basin is dominated largely by normal faulting and with a minor degree of vertical-dip-slip component. In contrast, in the Midland Basin the faulting is accommodated by a mix of normal and strike-slip faulting. Nonetheless, this color-coded ternary diagram provides an alternative approach and allows one to forecast the faulting type based on the inverted stress tensor.

It is worth noting that previous stress studies (Martínez-Garzón et al., 2013; Schoenball et al., 2014) on the induced seismicity in geothermal fields have indicated that fluid injection around the injection site can alter the in-situ stress orientation and thus change the faulting pattern before and during the fluid injection. However, this change on the stress orientation does not lead to a fundamentally different faulting regime. Despite the fact that fluid-injection from both of SWD and HF-operation has been very active and densely populated in the Permian Basin for extended times, our previous seismotectonic studies and the newly determined focal mechanisms from this study show no temporal variation of the focal mechanism types for each cluster. Although there were only few historic focal mechanisms documented before the induced seismicity has become very active, we do not see a fundamentally different faulting type either (Figures 1

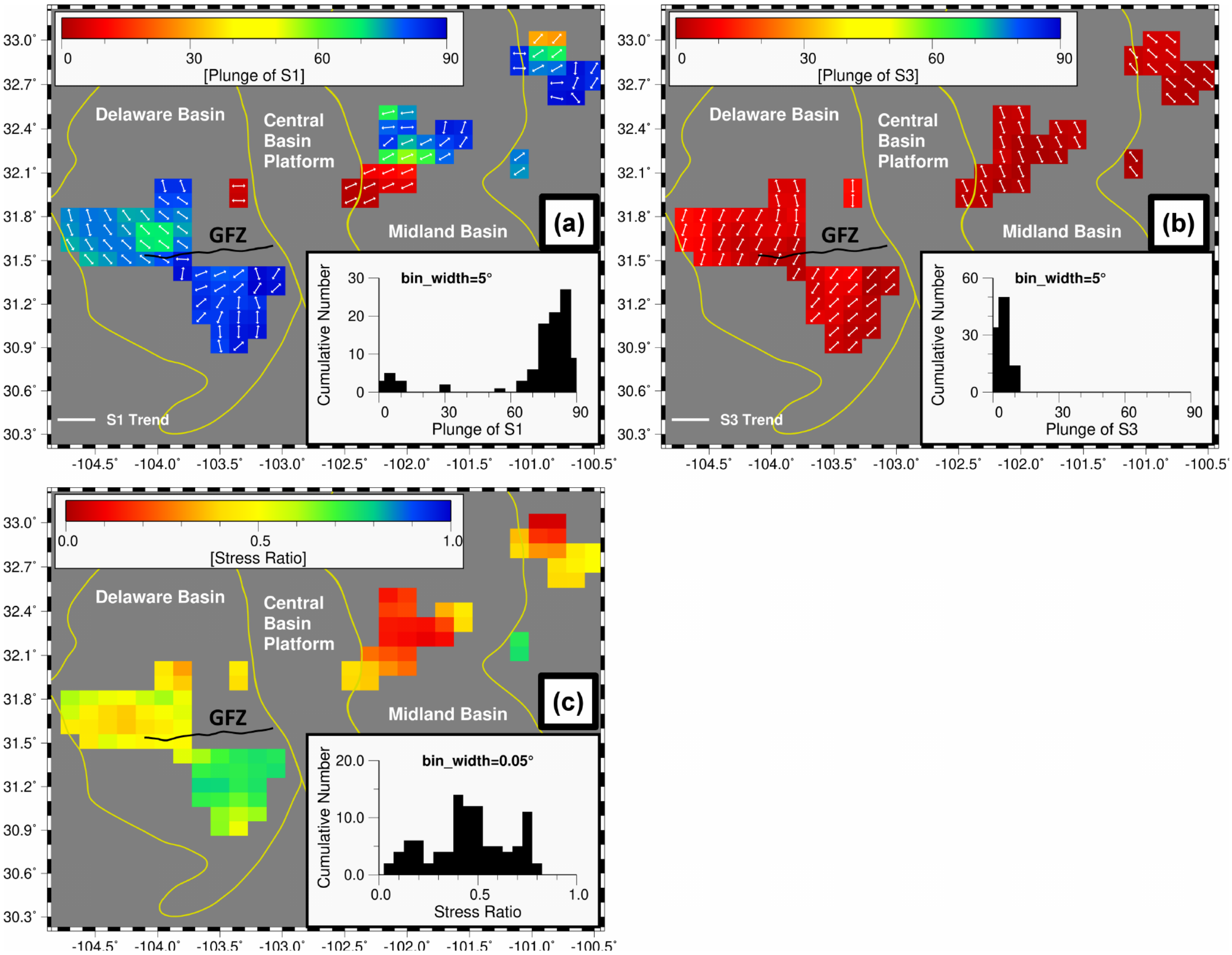

Figure 5 Stress parameters from the 2-D stress model: (a) the trends of S1 stacked on top of the color-coded plunge; (b) the trends of S3 stacked on top of the color-coded plunge; and (c) the spatial distribution and statistics of stress-ratio R. This figure shows a systematic S3 pattern in our study area, and suggests that S3 is the dominating stress. See the section 3 (Results - the inverted 2-D stress model) for details.

and 6).

Nonetheless, because the basin is currently under a heavy influence of fluid injection, the inverted stress model should be considered as a present-day stress field. Caution needs to be taken when using this inverted stress model.

4 Discussion – the 2-D distribution of seismic moment release and the tectonic implication

Among the several tens of thousands earthquakes that occurred in the Permian Basin of Texas since 2017, sixty-four M ≥ 4 earthquakes have been documented. Moreover, among those M ≥ 4 earthquakes, only seven earthquakes are larger than magnitude 5. In contrast to the widely distributed small-sized induced seismicity (e.g., M<4 or so), those M ≥ 4 earthquakes took place in a narrow zone that is seemingly transecting across the Permian Basin (Figure 1). Normal-faulting focal mechanisms dominate this zone. From 2017 to the present, the widely distributed seismicity together has thus released a significant amount of seismic moment, compared to that only three documented M ≥ 5 earthquakes occurred in the whole Permian Basin in 1931-2016 (U.S. Geological Survey (USGS), 2025). As mentioned above, the geodetic observations have indicated that parts of the Delaware Basin have experienced notable ground-surface subsidence after induced seismicity became very active in our study area (Figure 7a). Specifically, the subsidence is located in areas south of the GFZ, and there also appears to be a spatial correlation between the ground-surface subsidence and the induced seismicity. Staniewicz et al. (2020) and Hennings et al. (2023) suggested that the HF-operation at 2–3 km below the ground surface is likely the most responsible factor for the subsidence, mainly because of the reduction of hydrocarbons and pore-pressure. It is worth noting that SWD is also active in the same area where a series of basement-rooted faults have been reactivated (Huang et al., 2022). However, whether the subsidence is caused predominantly by the oil production activities (i.e., HF-operation) or other tectonic factors may have been involved, in our opinion, is debatable.

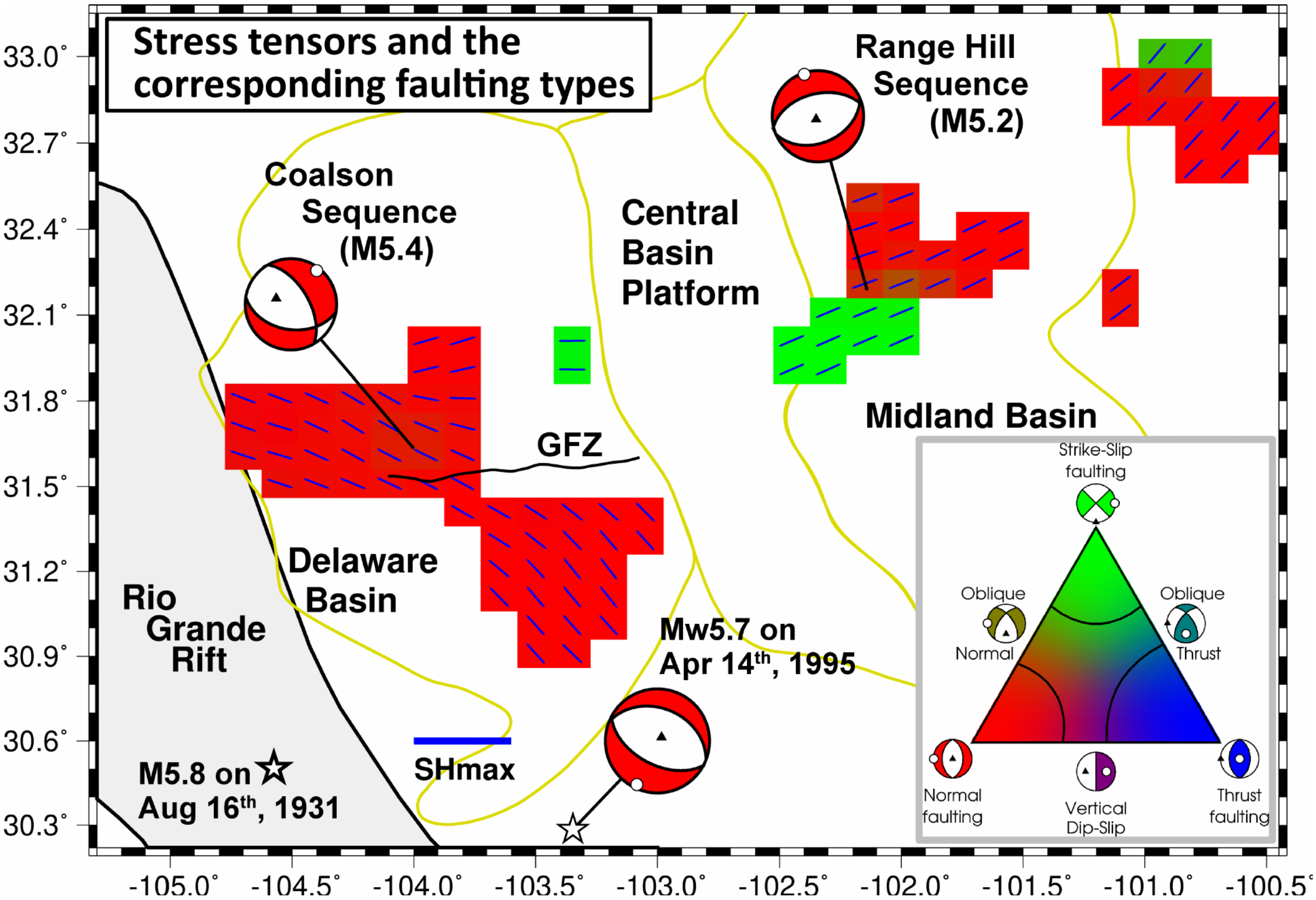

Figure 6 A composite figure shows the stress tensors and the corresponding faulting types represented by the color-coded ternary diagram (modified from Frohlich and Apperson, 1992). Most of our study area presents normal or oblique-normal faulting types whereas the strike-slip faulting is distinctively existing in the western part of the Midland Basin. Two focal mechanisms are of the M5.4 Coalson and the M5.2 Ranch Hill sequences, respectively. The focal mechanism shown at the bottom of the figure occurred on Apr 14th, 1995 (U.S. Geological Survey (USGS), 2025). The oil and gas activities were not active in that area at that time. It presents a similar faulting type with that of the current induced seismicity.

From Figure 7b, it has been clearly shown that the cumulative seismic moment release is dominated by a number of $M \geq 4$ earthquakes; several prominent earthquake groups having $M \geq 4$ earthquakes together make up nearly 79% of the Permian Basin's total seismic moment release (e.g., the seismic zones of the Coalson sequence in West Texas, the Range Hill sequence in the Midland Basin, as well as the Snyder area; Figure 1). We also observe a particular pattern of the cumulative seismic-moment release within the Delaware Basin: it is higher in areas north of the GFZ and lower in the south of the GFZ. Further, Figure 7c suggests that those seismicity groups with higher moment release also have a higher long-term seismic moment rate. As expected, the seismicity group containing the Coalson earthquake sequence has the highest cumulative seismic moment release as high as 1.4×10^{17} N-m, and the highest seismic-moment rate (i.e., the brightest spots in Figure 6b and c), which can be attributed to a large number of the $M \geq 4$ earthquakes. In particular, two $M \geq 5$ earthquakes from the Coalson sequence occurred nearly one year apart. This could mean that considerable seismic strain has been built up and preserved in this fault zone, implying this fault system may have been highly stressed over extended geological time. Combining the 2-D distribution of seismic-moment rates and *b*-values (Figure 7c and d), we notice that the *b*-values are around a level of $b = 1$ for those earthquake groups having higher seismic-moment release and seismic-moment rates. Within these areas, *b*-value was as high as 1.46 prior to the occurrence of those major $M \geq 5$ earthquakes (Huang et al., 2024). The presence of $M \geq 5$ earthquakes has thus statistically reduced the *b*-value down to the current level around $b = 1$, indicating that the moment release may have stabilized after the major $M \geq 5$ earthquakes occurred within these areas. However, the area within the Midland Basin containing the M5.2 Range Hill event currently has $b = 0.9$, slightly below the level of $b = 1.03$ determined for the whole Midland Basin (Huang et al., 2024). Nevertheless, it is not exceptionally low and still at the global level (Schorlemmer et al., 2005).

It is clear that a considerable amount of seismic-moment has been released by the induced seismicity within the Permian Basin; and yet, a conventional wisdom has indicated that seismic moment released by an earthquake is subject to the buildups of tectonic stress on pre-existing faults (Kanamori and Brodsky, 2004). Because there is no indication that cur-

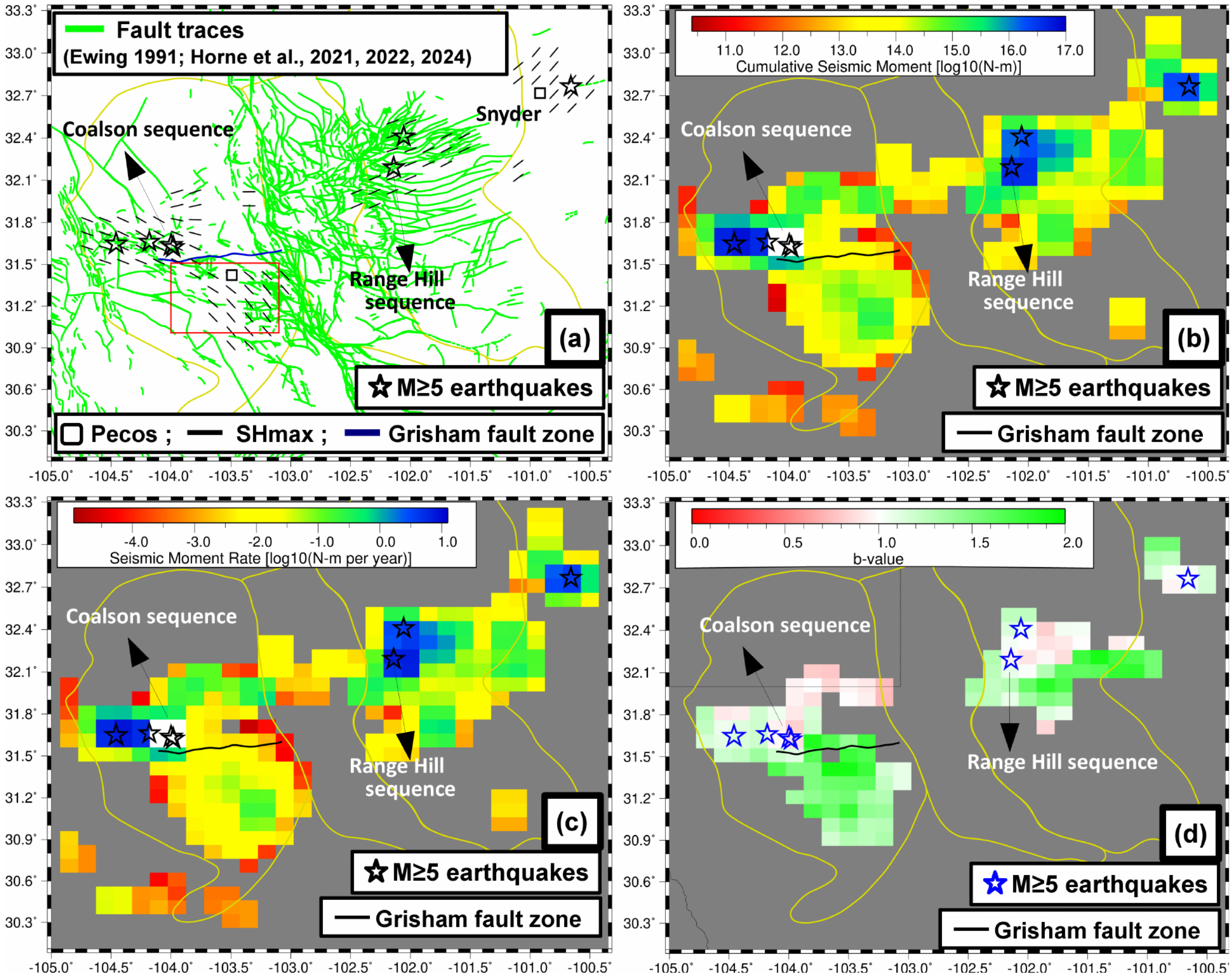

Figure 7 Figures show the characteristics of seismic deformation: (a) Distribution of the mapped fault traces (Ewing, 1991; Horne et al., 2021, 2022, 2024), and the inverted SHmax. The red lines display the area that has geodetically observed ground surface subsidence (Staniewicz et al., 2020) (b) Cumulative seismic-moment release; (c) Seismic-moment rate; (d) *b*-value. As expected, the highest moment-release and moment-rate are associated with the M ≥ 5 events, where *b*-value has reached a level of *b* = 1. See section 4 (Discussion – the 2-D distribution of seismic moment release and the tectonic implication) for detailed interpretation.

rently the greater Permian Basin is a dynamic tectonic regime (e.g., neither the current plate boundaries nor active continental collision that constantly accumulate seismic strain), the question regarding the seismogenic source (i.e., the stress source) of the released seismic strains clearly stands out. As summarized by Horne et al. (2021), the present-day fault architecture within the greater Permian Basin was initiated by a series of tectonic events, including the interactions between the Ancestral Rocky Mountain Orogeny and Ouachita Marathon Orogeny during the Late Mississippian to Early Permian (Dickinson and Lawton, 2003; Leary et al., 2017). Later, the post-Permian extensional tectonism collectively formed the present-day normal and strike-slip faulting structures, and the tectonic strain was thus preserved within these fault systems located in the pre-Cambrian basement. In addition to these widely distributed basement-rooted faults within the Permian Basin, notably, the Rio Grande Rift (located immediate west of our study area; Figures 1 and 6) also resulted from the past tectonism and is still active (Kelsch et al., 2025; Murray et al., 2019). This rift system features Quaternary faults, sedimentary basins, widespread volcanic activity, and thinned lithosphere. Currently, the crustal extension associated with the rift can be geodetically observed in regions immediately west of the GFZ (Murray et al., 2019). Given the tectonic history of these pre-existing normal faults, the widely distributed extensional crustal deformation and a systematic pattern of the stress field is unlikely caused solely by the current production activities (i.e., the HF-operation).

The gravitational collapse simply due to the disappearance of hydrocarbon bodies without reactivating nearby pre-existing faults would have caused subsidence locally (most likely in a form of aseismic slip), similar to the process for seismic events created by underground mining activities. However, hydrocarbon extraction in areas consisting of pre-existing faults can induce earthquakes by reactivating the pre-existing faults in two ways. First, during the HF-operation, pressurized fluid-injection (i.e., stimulation) is used to retrieve hydrocarbons. Similar to the process of SWD, the pressurized fluid should have the effect to reduce the normal stress and thus to reactivate pre-existing faults. Secondly, after the hydrocarbons were depleted in the reservoirs, decreased pore-fluid pressure will increase the effective normal stress which will eventually lead to an increase of fault asperities. Therefore, it will result in compaction of the pore-pressure reduced reservoir, and it can initiate the strain accumulation along the nearby faults because of the increased normal stress. Future seismicity occurs when the accumulated strain exceeds the increased threshold of fault reactivation , leading to an increased earthquake magnitude (Davis et al., 1995; Pennington et al., 1986).

Staniewicz et al. (2020) and Hennings et al. (2023) attributed the ground subsidence to mainly the reduction of hydrocarbon content. Lee et al. (2023) further demonstrated that both reservoir compaction (due to the reduction of hydrocarbon content) and fault reactivation near the hydrocarbon reservoir have jointly contributed to the geodetically observed ground deformation. Specifically, the fault-slip has a more dominant effect than the compaction does. Similarly, using the cumulative seismic moment release as a proxy for cumulative earthquake slip, Morris et al. (2024) have demonstrated that the cumulative slip in earthquakes resulting from fault reactivation account for a large portion of the subsidence. Furthermore, they suggested that the pressurized fluid-injection from both SWD and HF-operation have jointly reactivated the pre-existing faults. Morris et al. (2024) also pointed out that fault architecture plays a role in the amount of slip: larger slip tends to occur along a larger fault segment. Note that the typical duration of a HF-operation is a few weeks and the injected fluid will have to flow back to the ground surface, whereas SWD is continuously flooding the fluid into the reservoir and the fluid does not flow back to the ground surface. The long-duration fluid injection could trigger far-field poroelastic effect for areas away from the injection wells. Therefore, SWD is more likely to trigger systematic and large-scale fault reactivation, resulting in larger fault segments; whereas the faults reactivated during HF-operations are more segmented and have smaller faulting area (i.e., associated with less slip). Despite the fact that HF- and SWD-operations co-exist in parts of the south Delaware Basin and have jointly triggered fault reactivation at a local scale, SWD is considered as the dominant factor to reactivate pre-existing basement-rooted faults and thus trigger larger-sized earthquakes in the Permian Basin (Grigoratos et al., 2022; Woo and Ellsworth, 2023; Savvaidis et al., 2020).

Using the cumulative seismic moment release as a proxy to represent the scale of slip along the reactivated faults, it has been shown that the fluid injection related fault reactivation has resulted in spatially widespread crustal deformation in our study area, particularly in the crystalline basement (Figure 7b and c). The released seismic-moment is not simply a function of pore-pressure perturbation; instead, the fault architecture plays a more important role on the size of an earthquake than the injected pore-pressure does (Ge et al., 2024; Morris et al., 2024). Lengthy pre-existing faulting structures allow for larger rupture areas and slippages when the earthquakes occur (Wells and Coppersmith, 1994). In addition to the fault architecture, the released seismic moment is also a function of the accumulated strain on the fault. Because the effect of injected fluid is mainly reducing the normal stress to trigger fault reactivation, rather than creating seismic strain, the plausible source of seismic strain should be related to tectonic factors. As mentioned above, the past tectonism that created the Permian Basin was the stress source during the tectonic events, not only creating a series of basement-rooted faults but also building up tectonic strains. While there is no geodetic evidence suggesting current strain accumulation, the previously created tectonic strains have been preserved in the lithosphere. Figure 7a-c show that the areas having a higher moment release (north of the GFZ) contain a well-developed fault system that was mapped by Ewing (1991); Horne et al. (2021, 2022, 2024). These broadly distributed basement-rooted fault systems were pre-stressed for an extended geological time. We hypothesize that the existence of the basement-rooted faults along with the preserved tectonic strain constitute a “strain-reservoir”, providing the source of seismic strain to be released during the earthquake sequence (Calais et al., 2016). Furthermore, the strain resulted from the ongoing lithosphere's thinning process within the Rio Grande Rift (i.e., thermal uplifting force) may have also incrementally contributed to the strain-reservoir at present time as well. Calais et al. (2016) further pointed out that the intraplate earthquakes triggered by a transient perturbation of stress field near the reactivated fault system tend to be clustered and in an episodic sequence. In the Permian Basin, the induced seismicity in areas having high seismic moment release are resembling the clustered and episodic swarm pattern, often with no clear distinction between foreshocks and aftershocks (Huang et al., 2022, 2024; Huang and Savvaidis, 2024).

5 Conclusions

Induced seismicity has allowed us to aim to map the present-day stress field at very fine resolution for the Permian Basin of Texas. With a total of 1591 well-constrained focal mechanisms, we have effectively achieved this goal. Our stress inversion results suggest a complex stress pattern in the Permian Basin. The Permian Basin is overall an extensional tectonic regime, as indicated by the predominant normal-faulting mechanisms and commonly middle/lower stress-ratios (around R = 0.4–0.6). Given the considerable seismic moment release, the widely distributed induced seismicity and their extensional stress pattern across the Permian Basin, the geodetically observed ground surface subsidence in parts of the Permian Basin of Texas is unlikely caused solely by the reduction of hydrocarbon bodies. Rather it is due to a systematic reactivation of dormant tectonic faults caused by fluid injection from both SWD and HF-operation. From a tectonic perspective, throughout time, induced seismicity within the Permian Basin has resulted in a widely distributed seismic deformation.

Acknowledgements

This paper has benefited from constructive comments made by two reviewers. Seismic data used in this study were processed using SAC software. All maps were generated by using GMT software (Wessel and Smith, 1991). This study was funded by the Texas Seismological Network and the Seismology Research, Bureau of Economic Geology, University of Texas at Austin. The authors also like to appreciate the State of Texas for funding the TexNet. Publication of this article was authorized by the Director of the Bureau of Economic Geology, University of Texas at Austin.

6 Data and code availability

All seismic waveform data we used can be accessed through both the Data Management Center of the Incorporated Research Institutions for Seismology and the TexNet web services of the International Federation of Digital Seismograph Networks (network code: TX; rtserve.beg.utexas.edu/fdsnws). Supplemental materials for this article include one table of the inverted stress axes; see the front page of the supplements for details. The computer codes for stress inversion can be accessed at https://www.usgs.gov/node/279402. Refer to Huang et al. (2022, 2024) and Huang and Savvaidis (2024) for the computer codes of waveform moment tensor inversions.

7 Competing interests

The authors acknowledge that none have a conflict of interest.

References

Anderson, E. The dynamics of faulting. *Transactions of the Edinburgh Geological Society*, 8(3):387–402, Jan. 1905. doi: 10.1144/transed.8.3.387.

Angelier, J. Determination of the mean principal directions of stresses for a given fault population. *Tectonophysics*, 56(3-4), 1979. doi: 10.1016/0040-1951(79)90081-7.

Barth, A., Reinecker, J., and Heidbach, O. Stress derivation from earthquake focal mechanisms. *World Stress Map Project Guidelines*, 12:1–12, 2008.

Bureau of Economic Geology. TexNet Earthquake Catalog. https://www.beg.utexas.edu/texnet/catalog, 2025. Accessed October 2025.

Calais, E., Camelbeeck, T., Stein, S., Liu, M., and Craig, T. J. A new paradigm for large earthquakes in stable continental plate interiors. *Geophysical Research Letters*, 43(20), Oct. 2016. doi: 10.1002/2016gl070815.

Calle, A. Z., Smye, K. M., Horne, E. A., Eastwood, R. L., Reedy, R. C., and Hennings, P. Lithofacies and porosity heterogeneity of Ordovician–Pennsylvanian successions of the Midland Basin: Implications for wastewater disposal reservoir potential. *AAPG Bulletin*, 108(12):2241–2286, Dec. 2024. doi: 10.1306/05212424005.

Chen, Y., Saad, O. M., Savvaidis, A., Zhang, F., Chen, Y., Huang, D., Li, H., and Aziz Zanjani, F. Deep Learning for P-Wave First-Motion Polarity Determination and Its Application in Focal Mechanism Inversion. *IEEE Transactions on Geoscience and Remote Sensing*, 62:1–11, 2024. doi: 10.1109/tgrs.2024.3407060.

Davis, S., Nyffenegger, P., and Frohlich, C. The 9 April 1993 earthquake in south-central Texas: Was it induced by fluid withdrawal? *Bull Seismol Soc Am*, 85:1888–1895, 1995. doi: 10.1785/BSSA0850061888.

Dickinson, W. R. and Lawton, T. F. Sequential intercontinental suturing as the ultimate control for Pennsylvanian Ancestral Rocky Mountains deformation. *Geology*, 31(7):609, 2003. doi: 10.1130/0091-7613(2003)031<0609:sisatu>2.0.co;2.

Ewing, T. E. The tectonic framework of Texas [accompanying text]. Technical report, University of Texas at Austin, Bureau of Economic Geology, 1991.

Frohlich, C. and Apperson, K. D. Earthquake focal mechanisms, moment tensors, and the consistency of seismic activity near plate boundaries. *Tectonics*, 11(2):279–296, Apr. 1992. doi: 10.1029/91tc02888.

Frohlich, C., DeShon, H., Stump, B., Hayward, C., Hornbach, M., and Walter, J. I. A Historical Review of Induced Earthquakes in Texas. *Seismological Research Letters*, 87(4):1022–1038, May 2016. doi: 10.1785/0220160016.

Ge, J., Nicot, J.-P., Smye, K. M., Calle, A. Z., Hennings, P., Horne, E. A., and Leng, J. Modeling the evolution of pore pressure from deep wastewater injection in the Midland Basin, Texas. *AAPG Bulletin*, 108(12):2287–2312, Dec. 2024. doi: 10.1306/09102424008.

Gephart, J. W. and Forsyth, D. W. An improved method for determining the regional stress tensor using earthquake focal mechanism data: Application to the San Fernando Earthquake Sequence. *Journal of Geophysical Research: Solid Earth*, 89(B11): 9305–9320, Oct. 1984. doi: 10.1029/jb089ib11p09305.

Grigoratos, I., Savvaidis, A., and Rathje, E. Distinguishing the causal factors of induced seismicity in the Delaware basin: Hydraulic fracturing or wastewater disposal? *Seismological Research Letters*, 93(5):2640–2658, Sept. 2022. doi: 10.1785/0220210320.

Hanks, T. C. and Kanamori, H. A moment magnitude scale. *Journal of Geophysical Research: Solid Earth*, 84(B5):2348–2350, 1979. doi: 10.1029/JB084iB05p02348.

Hardebeck, J. and Shearer, P. A New Method for Determining First-Motion Focal Mechanisms. *Bulletin of the Seismological Society of America*, 92(6):2264–2276, Aug. 2002. doi: 10.1785/0120010200.

Hardebeck, J. and Shearer, P. Using S/P Amplitude Ratios to Constrain the Focal Mechanisms of Small Earthquakes. *Bulletin of the Seismological Society of America*, 93(6):2434–2444, Dec. 2003. doi: 10.1785/0120020236.

Hardebeck, J. L. and Michael, A. J. Damped regional-scale stress inversions: Methodology and examples for southern California and the Coalinga aftershock sequence. *Journal of Geophysical Research: Solid Earth*, 111(B11), Nov. 2006. doi: 10.1029/2005jb004144.

Hennings, P., Staniewicz, S., Smye, K., Chen, J., Horne, E., Nicot, J.-P., Ge, J., Reedy, R., and Scanlon, B. Development of complex patterns of anthropogenic uplift and subsidence in the Delaware Basin of West Texas and southeast New Mexico, USA. *Science of The Total Environment*, 903:166367, Dec. 2023. doi: 10.1016/j.scitotenv.2023.166367.

Hennings, P., Ge, J., Horne, E. A., Smye, K. M., and Nicot, J.-P. Pore pressure thresholds associated with seismogenic fault slip in the Midland Basin, west Texas, United States. *AAPG Bulletin*, 108

(12):2347–2375, Dec. 2024. doi: 10.1306/07232424014.

Horne, E. A., Hennings, P. H., and Zahm, C. K. *Basement-rooted faults of the Delaware Basin and Central Basin Platform, Permian Basin, West Texas and southeastern New Mexico*. Apr. 2021. doi: 10.23867/ri0286c6.

Horne, E. A., Hennings, P. H., Smye, K. M., Staniewicz, S., Chen, J., and Savvaidis, A. Structural characteristics of shallow faults in the Delaware Basin. *Interpretation*, 10(4):T807–T835, Aug. 2022. doi: 10.1190/int-2022-0005.1.

Horne, E. A., Hennings, P., Smye, K. M., Calle, A. Z., Morris, A. P., and Huang, G.-C. D. Interpretation, characterization, and slip hazard assessment of faults in the Midland Basin, west Texas, United States. *AAPG Bulletin*, 108(12):2313–2346, Dec. 2024. doi: 10.1306/01242423080.

Huang, G.-C. D. and Savvaidis, A. Reactivated Seismogenic Faults and Earthquake Source Mechanisms in the Snyder Area of Texas. *Seismological Research Letters*, 95(6), 2024. doi: 10.1785/0220240048.

Huang, G.-C. D., Horne, E., Kavoura, F., and Savvaidis, A. Characteristics of Seismogenic Structures and 3D Stress State of the Delaware Basin of West Texas as Constrained by Earthquake Source Mechanisms. *Seismological Research Letters*, 93(6): 3363–3372, Aug. 2022. doi: 10.1785/0220220054.

Huang, G.-C. D., Chen, Y., and Savvaidis, A. Complex Seismotectonic Characteristics in the Midland Basin of Texas: Constrained by Seismicity and Earthquake Source Mechanisms. *Seismological Research Letters*, 95(3):1870–1884, Jan. 2024. doi: 10.1785/0220230269.

Huang, G. D., Savvaidis, A., and Walter, J. I. Mapping the 3-D Lithospheric Structure of the Greater Permian Basin in West Texas and Southeast New Mexico for Earthquake Monitoring. *Journal of Geophysical Research: Solid Earth*, 124(11):11466–11488, Nov. 2019. doi: 10.1029/2019jb018351.

Kanamori, H. and Brodsky, E. E. The physics of earthquakes. *Reports on Progress in Physics*, 67(8), 2004. doi: 10.1088/0034-4885/67/8/r03.

Kavoura, F., Savvaidis, A., and Rathje, E. Determination of local magnitude for earthquakes recorded from the Texas Seismological Network (TexNet). *Seismol. Res. Lett.*, 91(6):3223–3235, Nov. 2020. doi: 10.1785/0220190366.

Kelsch, J. M., Ricketts, J. W., Rodriguez-Gonzalez, G., Ma, L., and Dickerson, P. W. Rotation of crustal extension and narrowing of rift faulting in the southern Rio Grande rift, Trans-Pecos Texas. *Geosphere*, 21(5):841–863, Aug. 2025. doi: 10.1130/ges02829.1.

Leary, R. J., Umhoefer, P., Smith, M. E., and Riggs, N. A three-sided orogen: A new tectonic model for Ancestral Rocky Mountain uplift and basin development. *Geology*, 2017. doi: 10.1130/g39041.1.

Lee, H. P., Staniewicz, S., Chen, J., Hennings, P., and Olson, J. E. Subsurface deformation monitoring with InSAR and elastic inversion modeling in west Texas. *Geoenergy Science and Engineering*, 231(212299):212299, Dec. 2023.

Lund, B. and Townend, J. Calculating horizontal stress orientations with full or partial knowledge of the tectonic stress tensor. *Geophysical Journal International*, 170(3), 2007. doi: 10.1111/j.1365-246x.2007.03468.x.

Lund Snee, J.-E. Recent advances in characterizing the crustal stress field and future applications of stress data: perspectives from North America. *Geological Society, London, Special Publications*, 546(1):9–45, May 2024. doi: 10.1144/sp546-2023-195.

Martínez-Garzón, P., Bohnhoff, M., Kwiatek, G., and Dresen, G. Stress tensor changes related to fluid injection at The Geysers geothermal field, California. *Geophysical Research Letters*, 40 (11), 2013. doi: 10.1002/grl.50438.

Morris, A., Smye, K., and Hennings, P. Hydraulic Fracturing, Fault System Architecture, and the Details of Anthropogenic Earthquakes in the Post-Pennsylvanian Delaware Basin of West Texas. *Lithosphere*, 2024(Special 15), 2024. doi: 10.2113/2024/lithosphere_2024_116.

Murray, K. D., Murray, M. H., and Sheehan, A. F. Active Deformation Near the Rio Grande Rift and Colorado Plateau as Inferred from Continuous Global Positioning System Measurements. *Journal of Geophysical Research: Solid Earth*, 124(2):2166–2183, Feb. 2019. doi: 10.1029/2018jb016626.

Pennington, W., Davis, S., Carlson, S., DuPree, J., and Ewing, T. The evolution of seismic barriers and asperities caused by the depressuring of fault planes in oil and gas fields of south Texas. *Bull Seismol Soc Am*, 76:939–948, 1986. doi: 10.1785/BSSA0760040939.

Savvaidis, A., Young, B., Huang, G.-C. D., and Lomax, A. TexNet: A statewide seismological network in Texas. *Seismological Research Letters*, 90(4):1702–1715, June 2019. doi: 10.1785/0220180350.

Savvaidis, A., Lomax, A., and Breton, C. Induced Seismicity in the Delaware Basin, West Texas, is Caused by Hydraulic Fracturing and Wastewater Disposal. *Bulletin of the Seismological Society of America*, 110(5):2225–2241, Aug. 2020. doi: 10.1785/0120200087.

Schoenball, M., Dorbath, L., Gaucher, E., Wellmann, J. F., and Kohl, T. Change of stress regime during geothermal reservoir stimulation. *Geophysical Research Letters*, 41(4):1163–1170, Feb. 2014. doi: 10.1002/2013gl058514.

Schorlemmer, D., Wiemer, S., and Wyss, M. Variations in earthquake-size distribution across different stress regimes. *Nature*, 437(7058), 2005. doi: 10.1038/nature04094.

Simpson, R. W. Quantifying Anderson's fault types. *Journal of Geophysical Research: Solid Earth*, 102(B8):17909–17919, Aug. 1997. doi: 10.1029/97jb01274.

Smye, K. M., Yut, K., Reedy, R. C., Scanlon, B. R., Nicot, J.-P., and Hennings, P. Challenges with managing unconventional water production and disposal in the Permian Basin. *AAPG Bulletin*, 108(12):2215–2240, Dec. 2024. doi: 10.1306/08082424025.

Snee, J.-E. L. and Zoback, M. D. State of stress in areas of active unconventional oil and gas development in North America. *AAPG Bulletin*, 106(2):355–385, Feb. 2022. doi: 10.1306/08102120151.

Staniewicz, S., Chen, J., Lee, H., Olson, J., Savvaidis, A., Reedy, R., Breton, C., Rathje, E., and Hennings, P. InSAR Reveals Complex Surface Deformation Patterns Over an 80,000 km^2 Oil-Producing Region in the Permian Basin. *Geophysical Research Letters*, 47 (21), Nov. 2020. doi: 10.1029/2020gl090151.

U.S. Geological Survey (USGS). ANSS Comprehensive Earthquake Catalog (ComCat). https://earthquake.usgs.gov/earthquakes/search, 2025. Accessed October 2025.

Wells, D. L. and Coppersmith, K. J. New empirical relationships among magnitude, rupture length, rupture width, rupture area, and surface displacement. *Bulletin of the Seismological Society of America*, 84(4):974–1002, Aug. 1994. doi: 10.1785/bssa0840040974.

Wessel, P. and Smith, W. H. F. Free software helps map and display data. *Eos, Transactions American Geophysical Union*, 72(41): 441–446, Oct. 1991. doi: 10.1029/90eo00319.

Woo, J.-U. and Ellsworth, W. L. Reactivation of Precambrian faults by deep wastewater injection in Midland basin, Texas, and performance evaluation of Seismic Response Areas. *Bulletin of the Seismological Society of America*, 113(6):2543–2556, Dec. 2023. doi: 10.1785/0120230086.

Yang, W. and Hauksson, E. The tectonic crustal stress field and style of faulting along the Pacific North America Plate boundary in Southern California. *Geophysical Journal International*, 194 (1):100–117, July 2013. doi: 10.1093/gji/ggt113.